Modified $H_2V_3O_8$ to Enhance the Electrochemical Performance for Li-ion Insertion: The Influence of Prelithiation and Mo-Substitution

Daniela Söllinger,[a] Michael Karl,[a] Günther J. Redhammer,[a] Jürgen Schoiber,[a] Valérie Werner,[a] Gregor A. Zickler,[a] and Simone Pokrant*[a]

Nanostructured $H_2V_3O_8$ is a promising high-capacity cathode material, suitable not only for Li^+ but also for $Na+$, Mg^{2+}, and Zn^{2+} insertion. However, the full theoretical capacity for Li^+ insertion has not been demonstrated experimentally so far. In addition, improvement of cycling stability is desirable. Modifications like substitution or prelithiation are possibilities to enhance the electrochemical performance of electrode materials. Here, for the first time, the substitution of vanadium sites in $H_2V_3O_8$ with molybdenum was achieved while preserving the nanostructure by combining a soft chemical synthesis approach with a hydrothermal process. The obtained Mo-substituted vanadate nanofibers were further modified by prelithiation. While pristine $H_2V_3O_8$ showed an initial capacity of 223 mAh g^{-1} and a retention of 79% over 30 cycles, combining Mo substitution and prelithiation led to a superior initial capacity of 312 mAh g^{-1} and a capacity retention of 94% after 30 cycles.

Introduction

Today the implementation of renewable energy supply is an important task for society.[1,2] However, most renewable energy sources are intermittent in their energy supply.[1] In consequence they provide most electrical energy at times that are not necessarily aligned with demand. To overcome this mismatch one solution is stationary electrical energy storage to balance energy generation and demand on various time scales. In this context, efficient energy storage is a key element for the successful realization of the energy turn. Furthermore, the growth-rate of electronic devices demands the development of flexible and wearable energy storage devices.[3,4] One of the most promising electrochemical energy storage concepts relies on rechargeable batteries such as Li-ion batteries (LIB), as a very prominent example.[4,5]

Layered transition metal oxides are considered as a promising battery electrode material class, since they are redox active and provide open crystal structures for cation insertion.[6,7] A typical representative is V_2O_5 (VO), one of the most studied vanadium oxides for battery applications. It has an open orthorhombic crystal structure (space group *Pmmn*, No. 59) and a theoretical capacity of 443 mAh g^{-1} (for three lithium equivalents, $Li_3V_2O_5$).[8–10] However the high theoretical capacity of VO has not been demonstrated experimentally, mainly due to the limited specific surface area combined with low electrical conductivity. In addition, the material is known for its poor cycling stability.[11,12] To overcome these drawbacks, modifications have been carried out successfully. Both extrinsic changes of the electrode material, like composite formation with reduced graphene oxide (rGO), and intrinsic changes, for example, by substitution of vanadium sites, lead to enhanced electrochemical performance, which has already been shown in several publications.[13–17] Although improvements of the cycling performance were achieved (e.g., over 15% specific capacity increase by substitution with Mo), they have not been far-reaching enough to justify the implementation of VO in commercial LIBs.[17]

However, VO can be used as starting material to synthesize hydrated vanadium oxides frequently exhibiting mixed vanadium valence states.[3,18,19] $H_2V_3O_8$ (also written as $V_3O_7 \cdot H_2O$, HVO) is another promising cathode material belonging to the layered vanadium oxide class for LIB.[3,20,21] HVO has an orthorhombic crystal structure (space group *Pnam*, No. 62–6).[22] It consists of V_3O_8 layers, where each layer consists of edge- and corner-shared VO_6 octahedra and VO_5 square pyramids (see Figure 1a).[23–25] Table S1 gives a general overview over previous syntheses and studies of HVO for different insertion ions, since the open framework of HVO offers not only insertion possibilities for Li^+, but also for Na^+, Mg^{2+}, or Zn^{2+}.[21,23,26–28] Insertion occurs parallel to the *bc*-plane, highlighted in Figure 1a (view in *c*-direction) and Figure 1b (view in *b*-direction).

Due to its mixed vanadium valence states (V^{5+} and V^{4+} ions, with a ratio of 2:1), HVO exhibits higher electronic conductivity and better capacity retention without any modifications compared to VO.[25,29] Electrochemical intercalation of four lithium ions per formula unit into the structure in the voltage window between 1.5–4.2 V vs. Li/Li^+ leads to a theoretical

[a] D. Söllinger, M. Karl, Dr. G. J. Redhammer, Dr. J. Schoiber, V. Werner, Dr. G. A. Zickler, Prof. S. Pokrant
Chemistry and Physics of Materials
University of Salzburg
5020 Salzburg (Austria)
E-mail: Simone.pokrant@sbg.ac.at

Supporting information for this article is available on the WWW under https://doi.org/10.1002/cssc.202002757

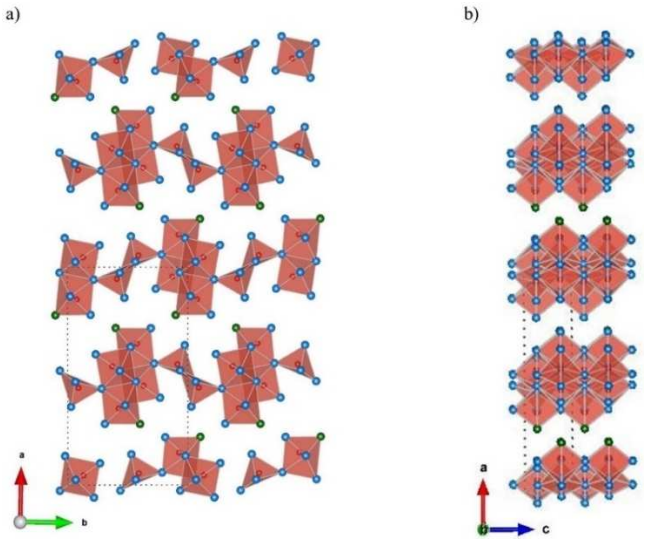

Figure 1. (a) $H_2V_3O_8$ crystal structure viewed along the *c*-direction. (b) $H_2V_3O_8$ crystal structure viewed along the *b*-direction. The dashed lines denote one unit cell. V-atoms are red, O-atoms belonging to H_2O bonds are dark green, all other O-atoms are blue.

capacity of 380–400 mAh g^{-1}, which is almost twice the amount of current commercially available cathode materials.[8,29] The reaction for Li-intercalation/deintercalation into HVO/HVO modifications is generally described by the following Equation (1):[3,30–32]

$$H_2V_3O_8 + x\,Li^+ + x\,e^- \rightleftharpoons Li_xH_2V_3O_8;\ (0 < x \leq 4) \quad (1)$$

The intercalation of 1 mol Li^+ into $H_2V_3O_8$ corresponds to a theoretical capacity of 94.77 mAh g^{-1}.

However, in the voltage window between 1.5–4.2 V vs. Li/Li^+, experimentally demonstrated discharge capacities of the cathode material HVO reach only 200–300 mAh g^{-1} for LIBs as a function of the applied current densities.[20,21,33] Nanostructured HVO materials (e.g., fibers) were obtained from VO precursors, followed by a hydrothermal process.[21,23,26,34] Nanostructuring is often beneficial for electrochemical properties because of an enhanced contact between electrode and electrolyte and between electrode material and conductive carbon, both leading to better electron and ion transport from/into the compound. Additionally, decreasing the particle size results in shorter electron/ion diffusion paths within the electrochemical active particles.[35] Extrinsic composite formation of HVO with carbon-containing compounds lead to improved electrochemical properties, such as increased capacities.[31,36] However, the full theoretical capacity of HVO has not been reached so far. In addition, cycling stability in HVO is still a challenge that needs to be addressed, to guarantee feasible long-living LIB.[3,8,21] Modifying the intrinsic composition and stabilizing the structure of electrode materials have proven to be successful approaches to overcome these problems, as demonstrated for VO.[12,17,37] Chemical prelithiation has been shown to be a successful strategy to increase cycling stability.[8,38,39] These positive effects of chemical prelithiation on stability and on the specific capacity of HVO have already been demonstrated in literature by Simões et al. and Xu et al.[8,40] However, substitution of vanadium by other cations, in analogy to VO, has not been reported so far for HVO. The standard approach to obtain substitution in oxides consists of mixing two oxide precursors in the desired ratio followed by annealing of this precursor mixture at high temperatures (typically above 800 °C) to allow for interdiffusion. However, this approach does not work for hydrated oxides since annealing leads to evaporation of crystal water and in consequence to mostly unfavorable phase changes. Furthermore, the nanostructure of HVO, for example, obtained via the hydrothermal process, needs to be preserved. This is difficult to guarantee during high-temperature annealing processes since sintering processes will occur, leading to larger particles.

In this study, we report for the first time a novel synthesis approach to obtain Mo-substituted HVO from modified VO precursor. This precursor was synthesized via a soft chemical approach introducing the substituting ion species (Mo^{6+}) into the VO structure. We demonstrate that the subsequent hydrothermal synthesis step can be adapted so that substituted HVO is obtained retaining the nanofiber morphology over the substitution level. Phase purity, single crystallinity, and homogenous distribution of Mo in the HVO nanofibers are confirmed by XRD, SEM, and TEM characterization. By combining Mo substitution in the HVO structure with chemical prelithiation, improved electrochemical properties are obtained. These properties are assessed by (long-time) galvanostatic cycling, cyclic voltammetry, and evaluation of the rate capability.

Results and Discussion

In order to substitute vanadium in the HVO structure, we chose to introduce the substituting ion on a V site of the precursor oxide VO. In contrast to HVO, VO exhibits V^{5+} sites exclusively. Therefore, the substituting ion has been chosen in relation to the properties of the V^{5+}-ion, that is, ionic radius (0.54 Å), coordination number (CN = 6), and oxidation state (5+). In addition, it should be redox active in order to preserve and potentially enhance the electrochemical activity. One of the suitable transition metal ions was molybdenum (Mo) in the oxidation state 6+ with an ionic radius of 0.59 Å (CN = 6).[41] In Figure 2, our synthesis strategy from VO over Mo-modified VO (VO-Mo) to Mo-modified HVO (HVO-Mo), and prelithiated Mo-modified HVO (Li-HVO-Mo) is summarized.

To incorporate Mo^{6+} into VO, the soft chemistry process leading to P-VO was modified by adding an aqueous solution containing the Mo^{6+} ion. Therefore, 1.77 g of $(NH_4)_6Mo_7O_{24}\cdot 4H_2O$ were dissolved in 100 mL deionized water to obtain an aqueous 0.1 M Mo-stock-solution. Various degrees of Mo incorporation were obtained by adjusting the respective amounts of Mo-solution and VO/oxalic acid suspension as listed in Table 1.

The samples were denoted according to the at % Mo replacing V in $(V_{1-y}Mo_y)_2O_{5-\delta}$ (VO-Mo) with VO-Mo-1, VO-Mo-2,

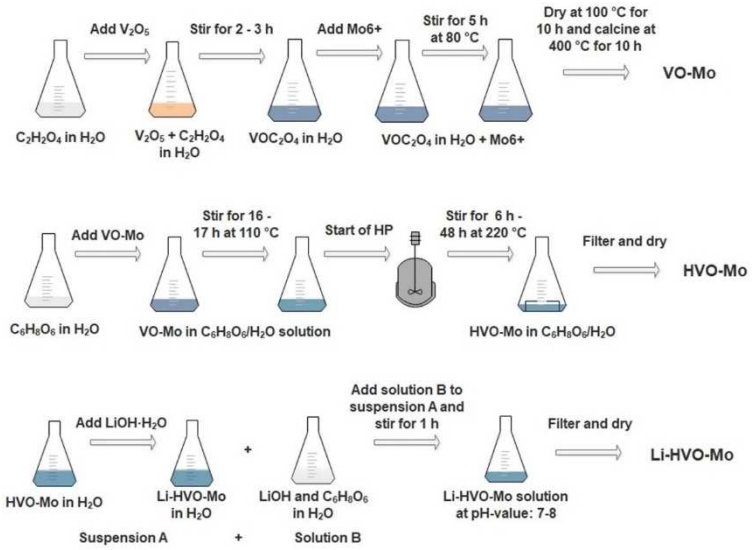

Figure 2. Synthesis process to obtain VO-Mo, HVO-Mo, and Li-HVO-Mo.

VO-Mo-5, VO-Mo-10, and VO-Mo-15 for $y = 0.01$, 0.02, 0.05, 0.1, and 0.15.

In the subsequent hydrothermal synthesis step the Mo-modified VO was used in the same molar quantities replacing P-VO. Temperature and pressure were kept constant in the autoclave, but the hydrothermal process time (HPT) was adjusted for each compound as listed in Table 1 in order to obtain single-phase material with a similar morphology as P-HVO. In analogy to VO-Mo, $H_2(Mo_yV_{1-y})_3O_{8-\delta}$ (HVO-Mo), was denoted HVO-Mo-1, HVO-Mo-2, HVO-Mo-5, and HVO-Mo-10 for $y = 0.01$, 0.02, 0.05, and 0.1. The reaction time had to be increased from 6 h (0 at% Mo) up to 60 h (10 at% Mo) (see Table 1). In addition, chemical prelithiation has been performed on HVO-Mo. The synthesis protocol to obtain chemical prelithiated HVO-Mo was similar to Li-HVO. The prelithiated, Mo-modified HVO compounds with the chemical formula $Li_xH_{2-x}(Mo_yV_{1-y})_3O_{8-\delta}$ (Li-HVO-Mo) were denoted Li-HVO-Mo-1, Li-HVO-Mo-2, Li-HVO-Mo-5, and Li-HVO-Mo-10 in analogy to HVO-Mo.

Phase purity, crystal structure, and composition of all compounds were determined by a combination of powder XRD, TEM/energy-dispersive X-ray spectroscopy (EDX) and SEM/EDX. The powder diffraction patterns and the lattice parameters obtained from Rietveld refinement of all VO-Mo compounds are displayed in Figures S2 and S3, respectively. VO-Mo compounds with up to 10 at% Mo content were single crystalline, exhibiting the same crystal structure as P-VO. Previous studies obtained phase-pure components of VO-Mo with up to 8 at% Mo content or a Mo/V ratio of about 1:9, respectively.[17,42] Nearly linear changes of the lattice parameters as a function of Mo content were observed, which approximates Vegard's law.[43] The lattice parameters *a* und *b* expanded linearly with the Mo content, while *c* shrank. In consequence, the unit cell volume was not affected strongly because the lattice parameter changes canceled out. Similar results have already been reported in previous studies.[42] In addition, change of color as a function of the Mo content indicated successful Mo incorporation into VO (Figure S4).

Powder diffraction patterns of the most characteristic HVO compounds, that is, P-HVO, HVO-Mo-5, Li-HVO, and Li-HVO-Mo-5, are displayed in Figure 3.

The diffraction patterns of all HVO-Mo and Li-HVO-Mo compounds are displayed in Figures S5 and S6. Some Bragg peaks, such as (310) and (020) for HVO-Mo (Figure S5) and (320) and (520) for Li-HVO-Mo (Figure S6), show intensity and shape changes with higher amounts of Mo content, proving that the presence of Mo in the structure had an influence on the obtained XRD pattern and overall on the crystal structure of HVO. Since the diffraction patterns of HVO-Mo and Li-HVO-Mo did not show any additional Bragg peaks compared to P-HVO und Li-HVO, we conclude that the obtained Li- and/or Mo-

Table 1. HVO-Mo synthesis: materials and adjusted hydrothermal process times (HPT) for P-HVO and HVO-Mo compounds.

Sample	VO [g]	$H_2C_2O_4$ [g]	0.1 M Mo-solution [mL]	Substitution degree [%]	HPT [h]
P-HVO	5.00	10.40	0	0	6
HVO-Mo-1	4.95	10.29	5.5	1	48
HVO-Mo-2	4.90	10.18	11.0	2	48
HVO-Mo-5	4.75	9.88	27.5	5	48
HVO-Mo-10	4.50	9.36	55.0	10	60

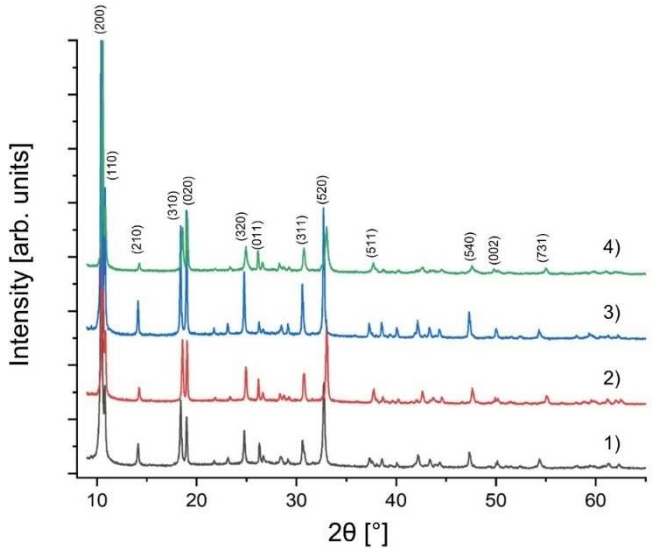

Figure 3. Powder diffraction pattern of 1) P-HVO (black), 2) Li-HVO (red), 3) HVO-Mo-5 (blue), 4) Li-HVO-Mo-5 (green). The Bragg peak positions of HVO in the 2θ [°] range are indexed for the Li-HVO-Mo-5 pattern space group *Pnam*.

modified materials are phase pure and exhibit the same crystal structure as the pristine materials.

The changes of the lattice parameters *a*, *b*, and *c* and of the unit cell volume upon Mo incorporation in HVO are summarized in Figure 4, as obtained by Rietveld refinements.

A monotonous change of all quantities as a function of Mo incorporation was observed, similar to VO-Mo. Mo incorporation up to 5 at% lead to a nearly linear increase of all lattice parameters. Such an increase, especially in the *a*-direction, enlarged the spacing between the V_3O_8 layers, providing better intercalation conditions for Li-ions. For higher amounts of substituted Mo (HVO-Mo-10) this linear relation was no longer valid. Not only the increase of the lattice parameters in comparison to HVO-Mo-5 was small, but also the crystalline quality decreased due to the high degree of substitution. This is not very surprising, since we do not expect a strict solid solution behavior by replacing a 5+ ion with a 6+ ion because of charge neutrality.[17,42] However, since all unit cell parameters and the unit cell volume increased monotonously with Mo incorporation, these results represent clear indications for successful Mo substitution in the HVO structure.

In addition, an assessment of the local (crystal) structure and composition was carried out by TEM and SEM. P-HVO consists of long fibers in the μm range with a width of around 80 nm (Figure S7a). High-resolution TEM (Figure S7b–d) showed that the P-HVO fibers were single-crystalline with an elongation directing along the [001] axis, which is consistent with current

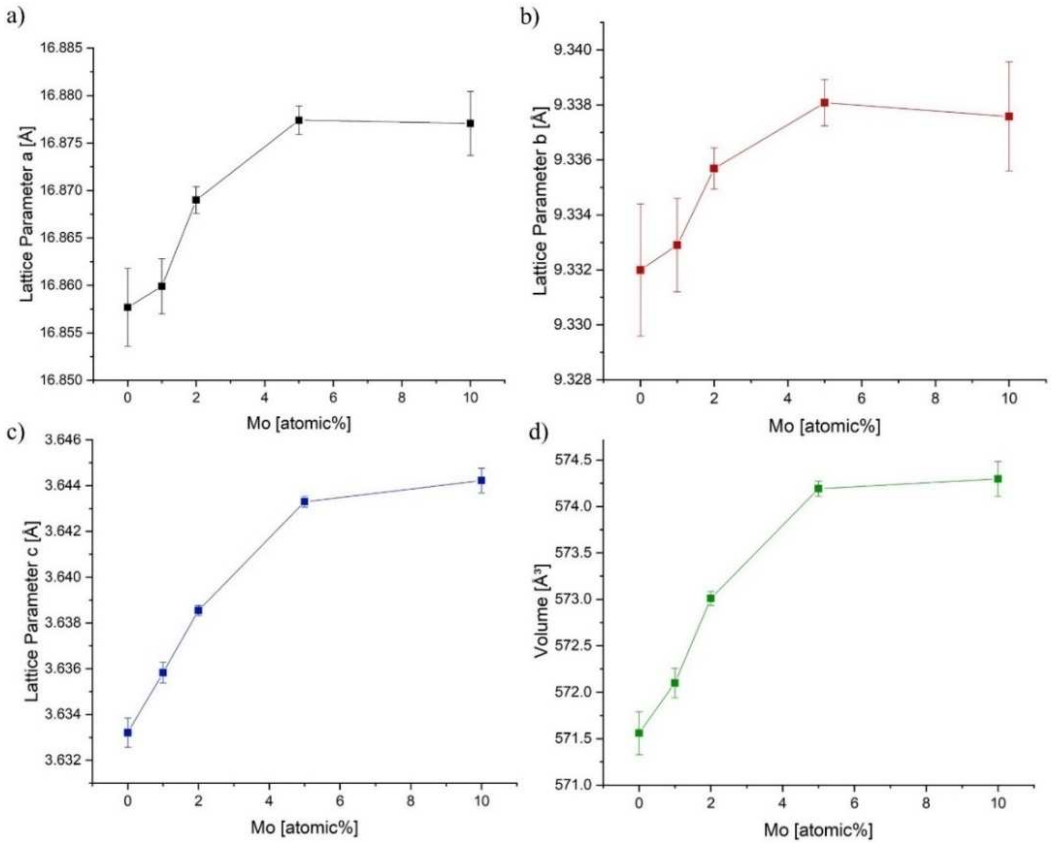

Figure 4. Lattice parameters of Mo substituted HVO compounds: a) *a*, b) *b*, and c) *c* direction and d) unit cell volume. Calculated error bars are presented in regard to the amount of Mo incorporation of the lattice parameters. The lines are a guide to the eye.

studies.[25,33] In Figure 5a an overview TEM image of HVO-Mo-5 is displayed.

The fiber morphology (crystallite size) was not affected by Mo substitution. In addition, the single-crystallinity of the fibers including the elongation direction in the [001] axis was confirmed as well, demonstrated in the high-resolution TEM image and its respective fast Fourier-transformation in Figure 5b–d. STEM/EDX (Figure S10) indicated a uniform distribution of Mo in the HVO-Mo-5 fiber. In addition, SEM/EDX measurements confirmed a uniform Mo distribution for all HVO-Mo modifications on a larger scale. The determined Mo and V content (in at %) corresponded to the values expected by stoichiometry (see Figure S11). These combined results of XRD, TEM, and SEM analysis gave evidence of vanadium substitution by Mo in the HVO structure for the first time, to our best knowledge.

In the next step the crystal structure of (Mo-substituted) HVO compounds was studied after prelithiation. Prelithiation of P-HVO led to lattice shrinkage in *a* und *b* and expansion in *c* direction, and in summary to a shrinkage of the unit cell volume of Li-HVO, as displayed in Figure S12 and Table S1. XRD measurements and full pattern analysis of Li-HVO-Mo compounds revealed a complex dependence of the lattice parameters *a*, *b*, and *c* as on Mo content, probably because of the competing effects of prelithiation (shrinkage) and Mo incorporation (expansion). However, the unit cell volume seems to follow a trend: it increases with Mo content similar to the HVO-Mo series, with the exception of Li-HVO-Mo-1. Therefore, we expect better conditions for Li-insertion in Li-HVO-Mo than in Li-HVO from a purely structural point of view, since larger interstitial spacing facilitates insertion.

Finally, the morphology of all compounds was determined by SEM and N_2 sorption. Figure 6 shows SEM micrographs of P-HVO and all HVO-Mo compounds. In Figure 6a,b it can be seen clearly that the fiber morphology, already observed by TEM for a very limited amount of fibers, is consistent over a larger amount of material. The nanofibers agglomerate and form a maze-like structure (Figure 6a). The fiber morphology was retained despite of Mo substitution, since no morphological changes were observed by SEM comparing P-HVO, HVO-Mo-1, HVO-Mo-2, HVO-Mo-5, and HVO-Mo-10 (see Figure 6b–f). However, grinding affected the morphology, since the long fibers were broken into pieces as shown in Figure S13c–f for P-HVO, HVO-Mo-5, Li-HVO, and Li-HVO-Mo-5 fibers.

The general morphology, however, was preserved. Specific surface areas were measured via N_2-Sorption for all compounds. The comparability of the surface areas with $14.6 \pm 2.0\ m^2 g^{-1}$ in average confirmed that the morphology was not affected strongly by neither substitution nor prelithiation (Figure S14).

In order to investigate the influence of Mo substitution and/or prelithiation on the electrochemical properties of HVO, phase-pure P-HVO and modified HVO compounds were tested electrochemically in a half-cell setup with Li metal as reference electrode. Even though HVO contains crystal water bonded to vanadium ions, no HF formation during cycling using $LiPF_6$ containing electrolytes was reported.[3,18] All materials were first discharged to 1.7 V vs. Li/Li^+ and afterwards charged to 3.9 V vs. Li/Li^+ with a constant current of $100\ mA\,g^{-1}$ for 30 cycles.

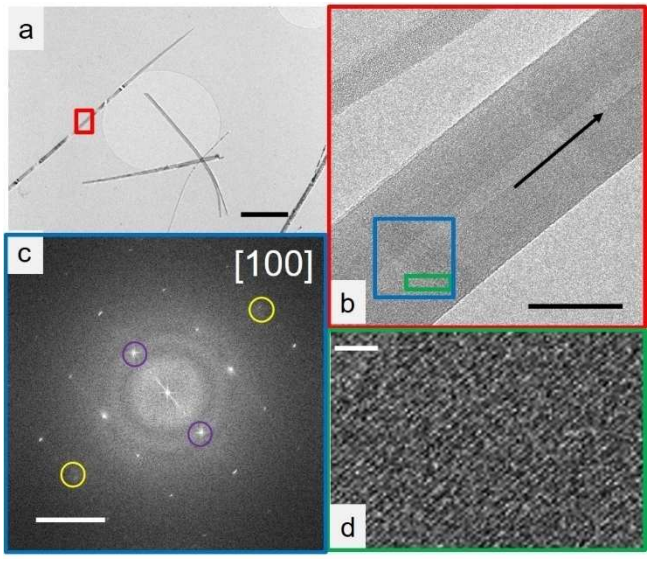

Figure 5. TEM-images: (a) Overview image of HVO-Mo-5 nanofibers (scale bar: 1 μm). (b) High-resolution TEM image of the red area in (a) (scale bar: 50 nm). The black arrow points in the elongation direction of the nanofiber [001]. (c) Fast Fourier-transformation of the blue area in (b) (scale bar: 2 nm) indexed with HVO structure in [100] zone axis (see simulated diffraction pattern in Figure S9). Yellow circles denote the position of (002) planes and violet of (020) planes. (d) Magnified zone of green box in (b) showing lattice fringes (scale bar: 4 nm).

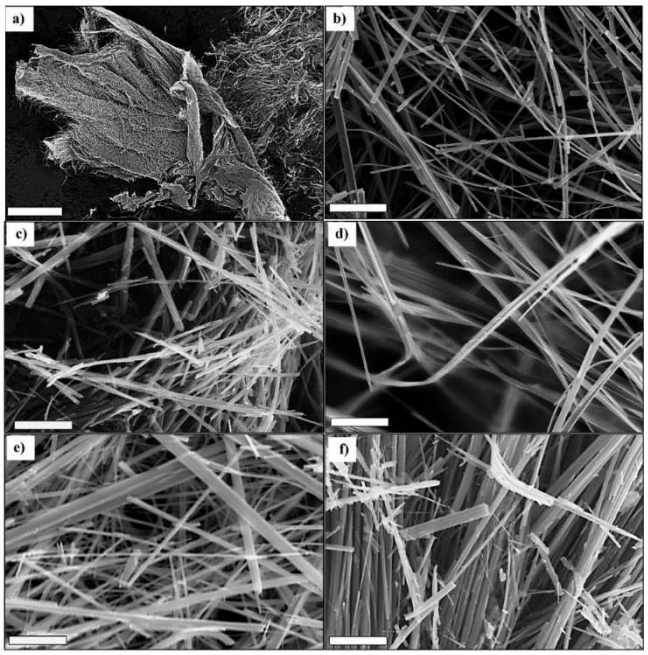

Figure 6. SE-SEM-images. (a) Overview over P-HVO nanowires (scale bar: 400 μm). (b) Zoom onto P-HVO nanowires (scale bar: 2 μm). (c) HVO-Mo-1 (scale bar: 2 μm). (d) HVO-Mo-2 (scale bar: 2 μm). (e) HVO-Mo-5 (scale bar: 2 μm). (f) HVO-Mo-10 (scale bar: 2 μm).

For all HVO modifications, substitution led to enhanced electrochemical properties with respect to capacity and cycling stability (see Figure S15). HVO-Mo-2 and HVO-Mo-5 components showed the highest increase of the specific capacity, probably as a consequence of the increased lattice parameters in comparison to P-HVO and HVO-Mo-1. It has been reported before that larger spacing facilitated the insertion of Li-ions into and out of the structure during cycling, which can improve the electrochemical properties, as recently discussed by Yao et al.[39] HVO-Mo-10 showed lower specific capacities, although the increase of the unit cell volume was larger than for HVO-Mo-2 and HVO-Mo-5. It is very likely that the diminished crystalline quality of HVO-Mo-10 canceled out potential positive effects of the enlarged crystal lattice.

Similarly to Mo substitution, prelithiation of HVO lead to improved electrochemical performance. The presence of electrochemically active Li-ions in the prelithiated cathode materials was demonstrated exemplarily for Li-HVO-Mo-5 by measuring the capacity of the half-cell in charge mode before the insertion of Li-ions during the first discharge (see Figure S16). In contrast to HVO-Mo, the lattice parameters and the unit cell volume of Li-HVO are lower compared to P-HVO (see Table S1 and Figure S12). Prelithiation is known for affecting physicochemical properties, outweighing structural arguments, as demonstrated for several materials and crystal structures.[39] Preintercalation led to improved conductivity due to the presence of mobile Li-ions in the materials, which compensated the ion loss during the initial cycle due to the formation of the solid–electrolyte interphase (SEI).[39] Furthermore, because of the intercalation and deintercalation of Li-ions into/from the materials during charge/discharge processes, the structures underwent undesired expansion/shrinkage associated with internal strain/stress. The so-called lattice breathing caused the structures to collapse over time, which led to an irreversible capacity fading. However, prelithiation reduced such negative impact and thus improved the electrochemical performance, especially the rate stability. In this context, Tian et al. showed for a HVO-related compound, prelithiated V_6O_{13} nanosheets, that the structural changes after the intercalation of Li-ions were less pronounced in comparison to non-prelithiated V_6O_{13}, which indicated a reduction of the negative effects of lattice breathing.[38] We believe that these improvements are at the origin of the electrochemical performance improvements of Li-HVO compared to P-HVO (Figure 7a), which showed an increase of the capacity retention due to the higher conductivity, and an increase of the specific capacity due to initial presence of Li-ions inside the battery system.

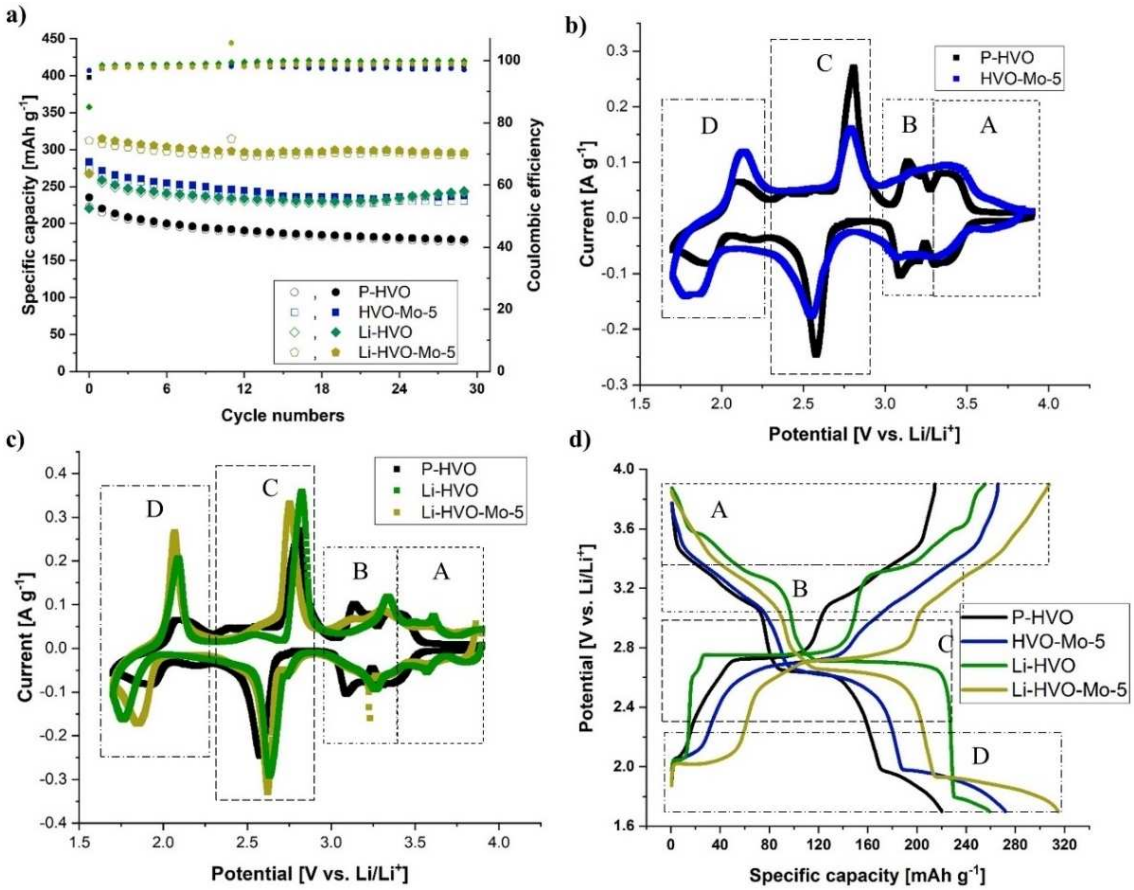

Figure 7. Electrochemical properties of P-HVO (black), Li-HVO (green), HVO-Mo-5 (blue), and Li-HVO-Mo-5 (yellow) in the potential range 1.7–3.9 V vs. Li/Li^+. a) Cycling performance and coulombic efficiency at 100 mA g^{-1} current density. b) Cyclic voltammograms of P-HVO and HVO-Mo-5 at a sweep rate of 0.1 mV s^{-1} recorded after the initial cycle. c) Cyclic voltammograms of P-HVO, Li-HVO, and Li-HVO-Mo-5 at a sweep rate of 0.1 mV s^{-1} recorded after the initial cycle. d) Charge and discharge curves of the initial cycle.

The electrochemical performance of Li-HVO-Mo compounds illustrates that the positive effects of prelithiation and Mo substitution are cumulative on the electrochemical properties. All Li-HVO-Mo materials showed improved performance apart from Li-HVO-Mo-10 (see Figure S17) compared to P-HVO. The best performance was observed for Li-HVO-Mo-5 (see Figure 7a). By cumulating the effects of prelithiation and Mo substitution (Li-HVO-Mo-5) a substantial capacity increase of 40% with respect to P-HVO was obtained, corresponding in good approximation to the sum of the capacity gain of Li-HVO (20%) and HVO-Mo-5 (23%). In addition, we found the highest capacity retentions after five and 30 cycles for Li-HVO-Mo-5, resulting in 67% capacity increase compared to P-HVO after 30 cycles. The advantage of improved capacity retention of Li-HVO-Mo-5 with respect to P-HVO was preserved even after 100 cycles (Figure S18).

In order to compare the performance, we focused on the capacities of the first, the 5th, and the 30th cycle as displayed in Table 2. The initial capacity of P-HVO as well as the capacity retention after 30 cycles is in good agreement with previous studies.[4,20]

Referring to Equation (1), a maximum of 4 mol Li^+ can be intercalated between 4.2 and 1.5 V vs. Li/Li^+ into HVO, reaching a capacity of approximately 380–400 mAh g^{-1}.[8,29] Therefore, the intercalated lithium equivalents amount to 2.3 for P-HVO, 2.9 for HVO-Mo-5, 2.8 for Li-HVO, and 3.3 for Li-HVO-Mo-5, respectively.

Table 3 compares the electrochemical performance of Li-HVO-Mo (initial capacity and capacity retention) with previous studies on HVO and HVO modifications. Depending on the potential window and the current densities, HVO nanobelts and HVO nanowires show smaller initial capacities in comparison to Li-HVO-Mo-5, whereas rGO/HVO exhibits either a higher capacity at the beginning but suffers from a lower capacity retention, or it exhibits a lower capacity at the beginning but has a similar/higher capacity retention in comparison to Li-HVO-Mo-5.[3,18,20,29,44,45] This demonstrates that Li-HVO-Mo provides improved electrochemical properties in comparison to several HVO modifications.

In order to analyze the intercalation properties as a function of Mo substitution and prelithiation we compared cyclic voltammetry (CV) (Figure 7b,c) and charge/discharge curves of P-HVO, HVO-Mo-5, Li-HVO and Li-HVO-Mo-5 (Figure 7d and Table 2). By CV measurements four reversible active redox couples were identified. The first two redox couples (A and B) were present between 3.9 and 3.0 V vs. Li/Li^+; the third between 3.0 and 2.2 V vs. Li/Li^+ (C), and the fourth was situated and in the range between 2.2 and 1.7 V vs. Li/Li^+ (D). This is comparable with current studies of HVO materials.[3,18,20,21] Mo substitution provoked subtle changes in the CV curve shape of redox couples A and B. They became less distinct and merged to one broad peak with negligible capacity change. Prelithiation, however, led to a shift of A and B towards higher potentials and to strongly increased capacities in the corresponding potential range. It is consistent that the improved ion conductivity triggered by prelithiation has an important effect at high potentials, where the cathode material is low on intercalated ions. Redox couple C exhibited capacity increase as a consequence of both prelithiation and Mo substitution. For redox couple D, a small shift to higher potentials was observed for Mo substitution accompanied by capacity increase, while prelithiation led to peak sharpening and capacity decrease. Since Mo substitution leads to enlarged lattice parameters, it seems consistent that the positive capacity effect is more important at lower potentials, when the Li sites in the cathode material are rather fully occupied. The opposite is true for prelithiation, which leads to lattice shrinking, which is unfavorable for full cathodes (i.e., low potentials). By combining Mo

Table 2. Electrochemical properties of P-HVO, HVO-Mo-5, Li-HVO, and Li-HVO-Mo-5. Capacities are indicated after the initial cycle.[a]

Sample	Capacity [mAh g^{-1}]	Capacity retention [%]		Capacity [mAh g^{-1}]		
		5th cycle	30th cycle	A, B	C	D
P-HVO	223	90	78	75	88	60
HVO-Mo-5	274	93	84	78	103	93
Li-HVO	268	90	90	98	129	41
Li-HVO-Mo-5	312	96	94	90	116	106

[a] A–D refer to various redox couples as seen in Figure 7 b,c and explained in the text below.

Table 3. Comparison of the electrochemical performance of Li-HVO-Mo-5 (present work) and HVO/HVO modifications from previous studies for LIBs.

Sample	Initial capacity [mAh g^{-1}]	Current density [mA g^{-1}]	Potential [V]	Capacity retention [%]	Ref.
Li-HVO-Mo	312	100	1.70–3.90	94 after 30 cycles	this work
HVO	212	200	1.50–4.00	90 after 50 cycles	[20]
HVO nanobelts	245	100	2.00–4.00	83 after 100 cycles	[45]
HVO nanowires	285	100	1.50–3.75	80 after 30 cycles	[18]
HVO single-crystal nanobelts	373	0.2 mA cm^{-2}	1.50–4.00	33 after 30 cycles	[32]
single-crystal HVO nanobelts	409	20	1.50–3.75	61 after 20 cycles	[46]
$V_3O_7 \cdot H_2O$@C nanoribbons	262	500	3.75–1.50	94 after 100 cycles	[29]
HVO/rGO-composite	268	100	3.75–1.50	93 after 50 cycles	[44]
rGO HVO film	377	100	1.50–3.50	65 after 30 cycles	[3]

substitution and prelithiation in Li-HVO-Mo-5 increased capacities were found in the potential regions of all four redox peaks because prelithiation added capacity in the high-potential region and Mo substitution in the low-potential region. This results in higher specific energy densities for modified HVO materials: 695.9 $Wh \cdot kg^{-1}$ (+20%) for HVO-Mo-5, 737.9 $Wh \cdot kg^{-1}$ (+27%) for Li-HVO, and 811.1 $Wh \cdot kg^{-1}$ (+40%) for Li-HVO-Mo-5) in comparison to P-HVO (579.2 $Wh \cdot kg^{-1}$), as shown in Figure S19.

Finally, in Figure 8 rate capability tests illustrate the higher specific capacities of Li-HVO-Mo-5 with respect to P-HVO at different charge/discharge currents. This indicated that the capacity improvement obtained by the synergistic effects of the modifications extended to rate capability.

Conclusion

A novel synthesis approach to enable substitution of the V site in hydrated vanadium oxides was proposed. The substitution of $H_2V_3O_8$ by Mo was demonstrated while retaining the crystal structure and the nanostructure of pristine $H_2V_3O_8$. Both are relevant for the electrochemical properties. This was enabled by performing substitution first in the V_2O_5 precursor. The two-step synthesis started with a soft chemistry reaction introducing Mo^{6+} into the V_2O_5 structure. In the next step Mo-substituted V_2O_5 was converted via a hydrothermal process to obtain Mo-modified $H_2V_3O_8$. Combining XRD and TEM characterization results proved that the obtained compounds were single-phase and single crystalline. The lattice parameters obtained by full pattern refinements in combination with the results of local chemical composition analysis indicated successful substitution of $H_2V_3O_8$ for the first time to our best knowledge. Therefore, Mo-modified compounds were denoted by the chemical formula $H_2(Mo_yV_{1-y})_3O_{8-\delta}$ with $y = 0.01$, 0.02, 0.05, and 0.1. Morphology characterization by SEM showed nanostructured fibers for pristine $H_2V_3O_8$ and for $H_2(Mo_yV_{1-y})_3O_{8-\delta}$, indicating that Mo substitution did not compromise the nanostructure. Prelithiation of $H_2(Mo_yV_{1-y})_3O_{8-\delta}$ did not affect the nanostructure either, but it led to unit cell contraction, which could be compensated partially by Mo substitution. The electrochemical properties of (modified) $H_2V_3O_8$ as cathode material in Li-ion batteries were evaluated by galvanostatic cycling, cyclic voltammetry, and rate capability measurements. Both Mo substitution and prelithiation improved the specific capacity and the cycling stability by the same order of magnitude. The combination of both modifications resulted in the addition of the positive effects. By comparing structural and electrochemical results on prelithiation and Mo substitution, we concluded that the positive effect of Mo substitution is based on lattice expansion, which facilitated Li insertion. This effect was active mainly at lower potentials. In contrast, prelithiation was found to add capacity preferentially at higher potentials, probably based on conductivity improvements and reduction of lattice breathing effects. In summary, the specific capacity of $Li_xH_{2-x}Mo_{0.15}V_{2.85}O_{8-\delta}$ (312 $mAh\,g^{-1}$) improved by 40% and the capacity retention after 30 cycles from 78 to 94% in comparison to $H_2V_3O_8$. In addition, $Li_xH_{2-x}Mo_{0.15}V_{2.85}O_{8-\delta}$ showed better long-time performance over 100 cycles and better rate capability than pristine $H_2V_3O_8$. By combining the presented intrinsic modifications with extrinsic modifications like composite formation with carbon-containing compounds, the performance of the HVO compounds might be further improved. The synthesis concept developed in this article has the potential to enable the incorporation of transition metal ions other than Mo^{6+} in the $H_2V_3O_8$ structure, potentially leading to further improvements of the electrochemical properties.

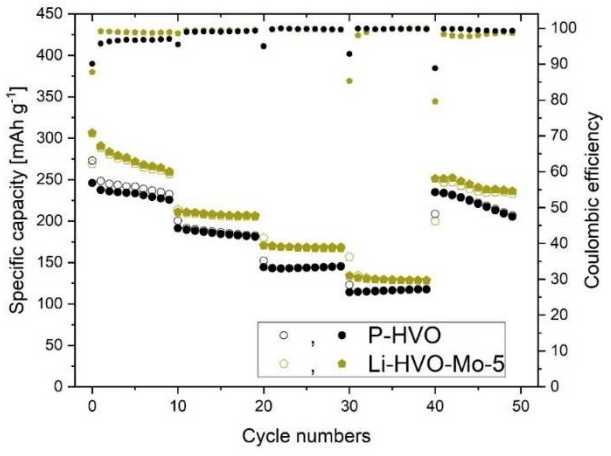

Figure 8. Specific capacity and coulombic efficiency of P-HVO (black) and Li-HVO-Mo-5 (yellow) in the potential range 1.7–3.9 V vs. Li/Li^+ at current densities of 100, 250, 500, and 1 $A\,g^{-1}$.

Experimental Section

Materials

Vanadium (V) oxide (V_2O_5, 99.2%), oxalic acid anhydrous ($H_2C_2O_4$, 98%), and L(+)-Ascorbic acid (99+ %) were purchased from Alfa Aesar. Ammonium molybdate tetrahydrate, $[(NH_4)_6Mo_7O_{24} \cdot 4H_2O$, 99.98%], 1.0 M $LiPF_6$ in ethyl carbonate/dimethyl carbonate (EC/DMC, 1:1 vol%) solution, lithium ribbon (99.9% trace metals basis), lithium hydroxide monohydrate ($LiOH \cdot H_2O$, 99.95%), and Whatman glass fibers (grade GF/D) were purchased from Sigma Aldrich. All chemical reagents were used as received.

Synthesis of $H_2V_3O_8$ and $Li_xH_{2-x}V_3O_8$

$H_2V_3O_8$ **(P-HVO)**: 10.4 g of $H_2C_2O_4$ was dissolved in 100 mL deionized water at room temperature.[37] After complete dissolution of the oxalic acid, 5 g V_2O_5 was added, followed by stirring for 3 h and further stirring at 80 °C for 5 h. The obtained solution was transferred into an evaporating dish and dried at 100 °C for 10 h followed by a calcination step at 400 °C for 10 h. 2 g of the obtained as-synthesized VO powder (P-VO) was added to 20 ml of a 0.025 M aqueous ascorbic acid solution. The obtained suspension was stirred under reflux at 110 °C for 16 h in a round-bottom flask. After this step, a hydrothermal process (HP) was initiated. The whole suspension was transferred into an autoclave with a 100 mL polytetrafluoroethylene (PTFE) inlet. Additionally, 30 mL deionized water was added to the suspension and brought to reaction at

220 °C for 6 h. The obtained precipitate was collected, washed with deionized water and isopropanol, and dried at 80 °C for 3 h. Pristine HVO without further modifications was denoted P-HVO.

$Li_xH_{2-x}V_3O_8$ **(Li-HVO)**: For chemical prelithiated HVO (Li-HVO), 0.5 g of as-synthesized P-HVO was suspended in 10 mL deionized water. In order to obtain a suspension (suspension A) with a pH-value of 7, 60 mg $LiOH \cdot H_2O$ was added. Parallel, a second solution (solution B) with a pH-value of 7 was prepared by dissolving 0.5 g ascorbic acid and 0.12 g $LiOH \cdot H_2O$ in 2 mL deionized water. Then solution B was added to suspension A. The final suspension was stirred at room temperature for 1 h and filtered. The collected product, with chemical formula $Li_xH_{2-x}V_3O_{8-\delta}$, was washed with water and isopropanol, and dried at 80 °C for 3 h.

$(V_{1-y}Mo_y)_2O_{5-\delta}$ (VO-Mo) and $Li_xH_{2-x}(Mo_yV_{1-y})_3O_{8-\delta}$ (Li-HVO-Mo): The syntheses of VO-Mo and Li-HVO-Mo are detailed in the Results and Discussion section.

Characterization

XRD: The crystalline phases of the synthesized powders were studied by XRD on a Bruker D8 Advance diffractometer having a goniometer radius of 280 mm and being equipped with a fast-solid-state LynxEye detector and an automatic sample changer. The measurements were carried out with $CuK_{\alpha 1,2}$ radiation in the 2θ range from 5 to 95° with a step size of 0.015°. All samples were prepared on zero-background single-crystal silicon sample holders. Full pattern refinement (Rietveld method) was performed with TOPASTM 4.2 (Version 4.2, Bruker AXS Inc., WI, USA).[47] The three-dimensional visualization of the crystal structure was constructed via VESTA.[48]

N_2 sorption: Nitrogen sorption isotherms were obtained with a Micromeritics ASAP 2420 sorption apparatus at −196 °C. Degassing of the samples was conducted at 80 °C for 12 h. The specific surface areas (SSA, m^2g^{-1}) were determined using the Brunauer-Emmett-Teller (BET) method.[49]

Electron microscopy: The morphology of the powders was characterized with a Zeiss Ultra Plus SEM using an in-lens secondary electron detector with an acceleration voltage between 5–10 kV and a JEOL-JEM-F200 TEM equipped with a cold field emission gun at an acceleration voltage of 200 kV. The TEM was equipped with high-angle annular dark-field (HAADF) detector used in scanning mode (STEM) and a large windowless JEOL Centurio EDX detector (100 mm^2, 0.97 srad, energy resolution $<$ 133 eV). The (modified) HVO samples for TEM analysis were prepared by depositing an isoproanolic suspension of the compounds onto holey carbon copper grids. The simulation of the diffraction patterns was carried out using the JEMS software.[50]

Electrochemical testing: For the electrode preparation 60 wt % of the electroactive material (60 mg), 30 wt% of carbon black (30 mg), and 10 wt% of polyvinylidene fluoride (PVDF) (10 mg) were ground and afterwards suspended in 2 mL toluene/THF (1:1, *v/v*). The prepared slurry was drop-casted on a titanium current collector, with a geometric surface of 1.3 cm^2, and dried for 4 h at 80 °C in a vacuum oven. Whatman glass fibers as separator, a 1.0 M solution of $LiPF_6$ in EC/DMC (1:1 vol %) as electrolyte and a disc of metallic lithium foil as counter and reference electrode were used for the half-cell setup. Photographs of the battery cell parts are displayed in Figure S1. The batteries were assembled in an argon filled glovebox ($<$ 0.1 ppm H_2O and $<$ 0.1 ppm O_2) and electrochemical tests were carried out using an 8 channel Astrol BAT-SMALL potentiostat. Capacities based on the mass load of the active material were determined by galvanostatic charge/discharge cycling with constant current. All galvanostatic measurements were carried out in the voltage range of 1.7–3.9 V (vs. Li/Li^+) at a current density of 100 $mA\,g^{-1}$, with the exception of long-term cycling tests (with 100 cycles). Parameter were set in the voltage range of 1.7–3.9 V (vs. Li/Li^+) at a current density of 500 $mA\,g^{-1}$. Cyclic voltammetry was measured in the voltage range of 1.7–3.9 V (vs. Li/Li^+) with a scanning rate of 0.1 $mV\,s^{-1}$. All measurements were carried out at ambient conditions.

Associated content

Figures of the setup of the battery cell, powder diffraction patterns of VO and HVO modifications, additional SE-SEM and TEM images of HVO and HVO modifications, specific surface areas from nitrogen sorption measurements, and further electrochemical properties of HVO and HVO modifications are reported in the Supporting Information.

Acknowledgements

TEM measurements were carried out on a JEOL JEM F200 TEM, funded by Interreg Österreich – Bayern 2014–2020 Programm-AB29 – "Synthese, Charakterisierung und technologische Fertigungsansätze für den Leichtbau "n2 m" (nano-to-macro)". The authors gratefully acknowledge M. Suljic for nitrogen sorption measurements, G. Tippelt for X-ray diffraction measurements and M. Simoes for advice on the HVO synthesis.

Conflict of Interest

The authors declare no conflict of interest.

Keywords: electrochemistry · $H_2V_3O_8$ · hydrothermal synthesis · Li-ion battery · synthesis design

[1] T. M. Gür, *Energy Environ. Sci.* **2018**, *11*, 2696–2767.
[2] F. Holtstiege, P. Bärmann, R. Nölle, M. Winter, T. Placke, *Batteries* **2018**, *4*, 4.
[3] Z. Liu, R. Xu, W. Wei, P. Jing, X. Li, Q. Zhu, H. Sun, Y. Dong, G. S. Zakharova, *Solid State Ionics* **2019**, *329*, 74–81.
[4] Z. Tian, N. Li, K. Xie, C. Niu, *J. Power Sources* **2019**, *417*, 14–20.
[5] M. Winter, B. Barnett, K. Xu, *Chem. Rev.* **2018**, *118*, 11433–11456.
[6] N. A. Chernova, M. Roppolo, A. C. Dillon, M. S. Whittingham, *J. Mater. Chem.* **2009**, *19*, 2526–2552.
[7] P. He, H. Yu, D. Li, H. Zhou, *J. Mater. Chem.* **2012**, *22*, 3680–3695.
[8] M. Simões, Y. Mettan, S. Pokrant, A. Weidenkaff, *J. Phys. Chem. C* **2014**, *118*, 14169–14176.
[9] Y. Yue, H. Liang, *Adv. Energy Mater.* **2017**, *7*, 1602545.
[10] W. Olszewski, I. Isturiz, C. Marini, M. Avila, M. Okubo, H. Li, H. Zhou, T. Mizokawa, N. L. Saini, L. Simonelli, *Phys. Chem. Chem. Phys.* **2018**, *20*, 15288–15292.
[11] Y. Yang, Y. Tang, G. Fang, L. Shan, J. Guo, W. Zhang, C. Wang, L. Wang, J. Zhou, S. Liang, *Energy Environ. Sci.* **2018**, *11*, 3157–3162.
[12] W. Bi, G. Gao, Y. Wu, H. Yang, J. Wang, Y. Zhang, X. Liang, Y. Liu, G. Wu, *RSC Adv.* **2017**, *7*, 7179–7187.
[13] Q. Liu, Z.-F. Li, Y. Liu, H. Zhang, Y. Ren, C.-J. Sun, W. Lu, Y. Zhou, L. Stanciu, E. A. Stach, J. Xie, *Nat. Commun.* **2015**, *6*, 6127.
[14] Y. Liu, Y. Wang, Y. Zhang, S. Liang, A. Pan, *Nanoscale Res. Lett.* **2016**, *11*, 549.
[15] Y. Tang, X. Rui, Y. Zhang, T. M. Lim, Z. Dong, H. H. Hng, X. Chen, Q. Yan, Z. Chen, *J. Mater. Chem. A* **2013**, *1*, 82–88.

[16] X. Huang, X. Rui, H. H. Hng, Q. Yan, *Part. Part. Syst. Charact.* **2015**, *32*, 276–294.
[17] H. Yu, J. Zeng, W. Hao, P. Zhou, X. Wen, *J. Nanopart. Res.* **2018**, *20*, 135.
[18] Q. An, J. Sheng, X. Xu, Q. Wei, Y. Zhu, C. Han, C. Niu, L. Mai, *New J. Chem.* **2014**, *38*, 2075–2080.
[19] H. Tang, N. Xu, C. Pei, F. Xiong, S. Tan, W. Luo, Q. An, L. Mai, *ACS Appl. Mater. Interfaces* **2017**, *9*, 28667–28673.
[20] S. Sarkar, A. Bhowmik, J. Pan, M. D. Bharadwaj, S. Mitra, *J. Power Sources* **2016**, *329*, 179–189.
[21] Y. Dai, Q. Li, S. Tan, Q. Wei, Y. Pan, X. Tian, K. Zhao, X. Xu, Q. An, L. Mai, Q. Zhang, *Nano Energy*. **2017**, *40*, 73–81.
[22] T. Y. Yoshio Oka, N. Yamamoto, *J. Solid State Chem.* **1990**, *89*, 372–377.
[23] M. Rastgoo-Deylami, M. S. Chae, S.-T. Hong, *Chem. Mater.* **2018**, *30*, 7464–7472.
[24] M. Rastgoo-Deylami, J. W. Heo, S. T. Hong, *ChemistrySelect* **2019**, *4*, 11711–11717.
[25] Y. Wu, X. Xu, C. Zhu, P. Liu, S. Yang, H. L. Xin, R. Cai, L. Yao, M. Nie, S. Lei, P. Gao, L. Sun, L. Mai, F. Xu, *ACS Energy Lett.* **2019**, *4*, 2081–2090.
[26] D. Wang, Q. Wei, J. Sheng, P. Hu, M. Yan, R. Sun, X. Xu, Q. An, L. Mai, *Phys. Chem. Chem. Phys.* **2016**, *18*, 12074–12079.
[27] Q. Pang, C. Sun, Y. Yu, K. Zhao, Z. Zhang, P. M. Voyles, G. Chen, Y. Wei, X. Wang, *Adv. Energy Mater.* **2018**, *8*, 1800144.
[28] Z. Cao, H. Chu, H. Zhang, Y. Ge, R. Clemente, P. Dong, L. Wang, J. Shen, M. Ye, P. M. Ajayan, *J. Mater. Chem. A* **2019**, *7*, 25262–25267.
[29] P. Liu, K. Bian, K. Zhu, Y. Xu, Y. Gao, H. Luo, L. Lu, J. Wang, J. Liu, G. Tai, *ACS Appl. Mater. Interfaces* **2017**, *9*, 17002–17012.
[30] H. Tang, N. Xu, C. Pei, F. Xiong, S. Tan, W. Luo, Q. An, L. Mai, *ACS Appl. Mater. Interfaces* **2017**, *9*, 28667–28673.
[31] P. Liu, K. Bian, K. Zhu, Y. Xu, Y. Gao, H. Luo, L. Lu, J. Wang, J. Liu, G. Tai, *ACS Appl. Mater. Interfaces* **2017**, *9*, 17002–17012.
[32] Y. Zhang, X. Liu, G. Xie, L. Yu, S. Yi, M. Hu, C. Huang, *Mater. Sci. Eng. B* **2010**, *175*, 164–171.
[33] H. Li, T. Zhai, P. He, Y. Wang, E. Hosono, H. Zhou, *J. Mater. Chem.* **2011**, *21*, 1780–1787.
[34] T. Hu, Y. Liu, Y. Zhang, M. Chen, J. Zheng, C. Meng, *Appl. Surf. Sci.* **2019**, *481*, 59–68.
[35] C. C. Li, B. Wang, D. Chen, L. Y. Gan, Y. Feng, Y. Zhang, Y. Yang, H. Geng, X. Rui, Y. Yu, *ACS Nano* **2020**, *14*, 531–540.
[36] C. Zhang, H. Song, C. Zhang, C. Liu, Y. Liu, G. Cao, *J. Phys. Chem. C* **2015**, *119*, 11391–11399.
[37] S. Y. Zhan, C. Z. Wang, K. Nikolowski, H. Ehrenberg, G. Chen, Y. J. Wei, *Solid State Ionics* **2009**, *180*, 1198–1203.
[38] X. Tian, X. Xu, L. He, Q. Wei, M. Yan, L. Xu, Y. Zhao, C. Yang, L. Mai, *J. Power Sources* **2014**, *255*, 235–241.
[39] X. Yao, Y. Zhao, F. A. Castro, L. Mai, *ACS Energy Lett.* **2019**, *4*, 771–778.
[40] X. Xu, Y.-Z. Luo, L.-Q. Mai, Y.-L. Zhao, Q.-Y. An, L. Xu, F. Hu, L. Zhang, Q.-J. Zhang, *NPG Asia Mater.* **2012**, *4*, e20.
[41] D. R. Lide, *Handbook of Chemistry & Physics*, *74th ed.*, CRC Press, Boca Raton, FL, **1993**.
[42] F. Haaß, A. H. Adams, T. Buhrmester, G. Schimanke, M. Martin, H. Fuess, *Phys. Chem. Chem. Phys.* **2003**, *5*, 4317–4324.
[43] L. Vegard, *Z. Phys.* **1921**, *5*, 17–26.
[44] K. Zhu, X. Yan, Y. Zhang, Y. Wang, A. Su, X. Bie, D. Zhang, F. Du, C. Wang, G. Chen, Y. Wei, *ChemPlusChem* **2014**, *79*, 447–453.
[45] L. Li, P. Liu, K. Zhu, J. Wang, J. Liu, J. Qiu, *J. Mater. Chem. A* **2015**, *3*, 9385–9389.
[46] S. Gao, Z. Chen, M. Wei, K. Wei, H. Zhou, *Electrochim. Acta* **2009**, *54*, 1115–1118.
[47] A. Coelho, *J. Appl. Crystallogr.* **2018**, 210–218.
[48] K. M. A. F. Izumi, *J. Appl. Crystallogr.* **2011**, *44*, 1272–1276.
[49] B. Stephen, P. H. Emmett, T. Edward, *J. Am. Chem. Soc.* **1938**, *60*, 309–319.
[50] P. Stadelmann, https://www.jems-swiss.ch/ accessed on January 16, **2020**.

Manuscript received: November 29, 2020
Revised manuscript received: December 18, 2020
Accepted manuscript online: December 18, 2020
Version of record online: January 5, 2021